Lower-Hybrid Drift Waves Driving Electron Nongyrotropic Heating and Vortical Flows in a Magnetic Reconnection Layer

L.-J. Chen,[1] S. Wang,[1,2] O. Le Contel,[3] A. Rager,[1] M. Hesse,[4] J. Drake,[2] J. Dorelli,[1] J. Ng,[1,2] N. Bessho,[1,2] D. Graham,[5] Lynn B. Wilson III,[1] T. Moore,[1] B. Giles,[1] W. Paterson,[1] B. Lavraud,[6] K. Genestreti,[7] R. Nakamura,[8] Yu. V. Khotyaintsev,[5] R. E. Ergun,[9] R. B. Torbert,[7] J. Burch,[10] C. Pollock,[11] C. T. Russell,[12] P.-A. Lindqvist,[13] and L. Avanov[1,2]

[1]*NASA Goddard Space Flight Center, Greenbelt, Maryland 20771, USA*
[2]*University of Maryland, College Park, Maryland 20747, USA*
[3]*CNRS/Ecole Polytechnique/Sorbonne Université/Univ. Paris Sud/Observatoire de Paris, Paris F91128, France*
[4]*University of Bergen, Bergen 5020, Norway*
[5]*Swedish Institute of Space Physics, Uppsala SE-75121, Sweden*
[6]*Institut de Recherche en Astrophysique et Planétologie, Université de Toulouse (UPS), CNRS, CNES, Toulouse 31027 Cedex 4, France*
[7]*University of New Hampshire, Durham, New Hampshire 03824, USA*
[8]*Space Research Institute, Austrian Academy of Sciences, Graz A-8042, Austria*
[9]*University of Colorado, Boulder, Colorado 80305, USA*
[10]*Southwest Research Institute, San Antonio, Texas 78238, USA*
[11]*Denali Scientific, Healy, Alaska 99743, USA*
[12]*University of California, Los Angeles, Los Angeles, California 90095, USA*
[13]*KTH Royal Institute of Technology, Stockholm SE-11428, Sweden*

(Received 10 October 2019; accepted 11 June 2020; published 9 July 2020)

We report measurements of lower-hybrid drift waves driving electron heating and vortical flows in an electron-scale reconnection layer under a guide field. Electrons accelerated by the electrostatic potential of the waves exhibit perpendicular and nongyrotropic heating. The vortical flows generate magnetic field perturbations comparable to the guide field magnitude. The measurements reveal a new regime of electron-wave interaction and how this interaction modifies the electron dynamics in the reconnection layer.

DOI: 10.1103/PhysRevLett.125.025103

The lower-hybrid drift instability (LHDI) is thought to be effective in plasma transport, e.g., [1–5], heating [6,7], and current dissipation [8–10] in systems where binary collisions are unimportant. It is driven by currents across the magnetic field in inhomogeneous plasmas [10]. During magnetic reconnection as the stored magnetic energy is released [11,12], both cross-field currents and spatial inhomogeneities are particularly strong in the core region of reconnection characterized by an intense electron current layer [13–16]. This region is referred to as the electron-scale reconnection layer. Such an environment is in principle conducive to the LHDI.

The role of LHDI in the electron-scale reconnection layer has not been experimentally established. The LHDI is widely considered to be important in magnetic reconnection by theories and simulations (see review by Fujimoto *et al.* [17]). However, detecting the LHDI in the electron-scale reconnection layer is highly challenging. Earlier laboratory [18,19] and space [20,21] measurements have only observed waves produced by the LHDI at the outer edge of the ion-scale reconnection current layers. One laboratory work showing waves in the lower-hybrid frequency range inside ion-scale reconnection layers only measured the magnetic field [22,23] and was not able to address the electrostatic aspect of the waves nor the electron response. In the laboratory experiment in [22,23], the probe is larger than the width of the electron-scale reconnection layer (approximately a few electron skin depths), and hence not able to resolve whether the waves could occur inside the layer. For space experiments, even though probe dimensions are orders of magnitude smaller than the electron skin depth, crossings of an electron-scale reconnection layer typically last for only a fraction of a second. Owing to the measurement time resolution, detection of the electron response to the waves could not be made until the Magnetospheric Multiscale (MMS) mission [24,25]. Our recent work suggests the presence of lower-hybrid drift waves (LHDW) in the electron-scale reconnection layer but the analyzed measurements (30 ms/sample) was insufficient to resolve the electron response [26]. In this Letter, we analyze the multidimensional structure of the wave electric field and its influence on electron distribution functions (7.5 ms/sample [27]). The measurements reveal a new regime of electron-wave interaction and the strong modification of electron dynamics in the reconnection layer.

Fully kinetic simulations predict that LHDWs can modify ion-scale current sheet properties and lead to onset of collisionless reconnection [7,28–31]. Electron heating

preferentially perpendicular to the magnetic field is shown to enhance the growth rate of the tearing instability responsible for reconnection onset by orders of magnitude [7,31]. Furthermore, the perpendicular heating is found to be nongyrotropic in a simulation [7]. These predictions have found no experimental evidence so far. On the other hand, the two-dimensional (2D) electric field structure of the LHDWs, predicted in the instability analysis [28,32,33] and simulations of ion-scale current sheets [34], has been observed at a plasma boundary without magnetic reconnection [35].

Here, we discuss LHDWs driving electron heating and flow vortices in an electron-scale reconnection layer observed by multiple MMS spacecraft. The size of the flow vortices is comparable to the width of the electron layer. In the layer, the magnetic field component antiparallel to the direction of the current (known as the guide field) dominates. The waves have a strong electrostatic component. The wave electric field perpendicular to the magnetic field results in vortical flow patterns that produce magnetic field perturbations comparable to the guide field magnitude. Electron acceleration by the wave electric field results in perpendicular and nongyrotropic heating. The measurements used in this Letter are taken by the following instruments: dc-coupled magnetic fields by the flux gate magnetometer [36], ac-coupled magnetic fields the search coil magnetometer [37], electric fields the electric double probes [38,39], and plasma measurements the fast plasma investigation [40].

The electron-scale reconnection current layer is encountered by MMS on the night side of the terrestrial magnetosphere at $\sim 18 R_E$ from the Earth at approximately 05:27:07 UT on 03 July 2017. A key signature of magnetic reconnection is the correlated reversals of the reconnected magnetic field B_N and the plasma outflows V_L, as illustrated in Fig. 1(a), where L is along the outflow, M is the direction of the reconnection current, and N completes the third orthonormal direction [26]. The correlated reversals are captured by MMS1 as shown in Figs. 1(b) and 1(c). In the two-second interval, B_N evolves from +3 to −4 nT [Fig. 1(b)], and the reversal is in concert with reversals of the electron and ion outflows, V_{eL} and V_{iL} [Fig. 1(c)]. At the location of the correlated reversals, the current is mainly carried by the electron flow, indicative of the electron-scale reconnection layer. The half-width of the electron current layer is estimated to be 25 km $\sim 2.8 d_e$, where $d_e = c/\omega_{pe} \sim$ 8.8 km is the electron skin depth based on the upstream density [41], c is the speed of light, and ω_{pe} is the electron plasma frequency. The estimate is established by $B_L/(\Delta B_L/\Delta N)$. Two ways to obtain the gradient $\Delta B_L/\Delta N$ are based on: (a) B_L and N from the MMS1 and MMS3 spacecraft [relative locations along N illustrated as the origins of arrows in Figs. 3(a) and 3(b)]; (b) $\mu_0 J_M$ (with negligible $\Delta B_N/\Delta L$) measured by MMS1 before the B_N reversal when the spacecraft enters the most intense V_{eM} layer. The two estimates yield consistent results.

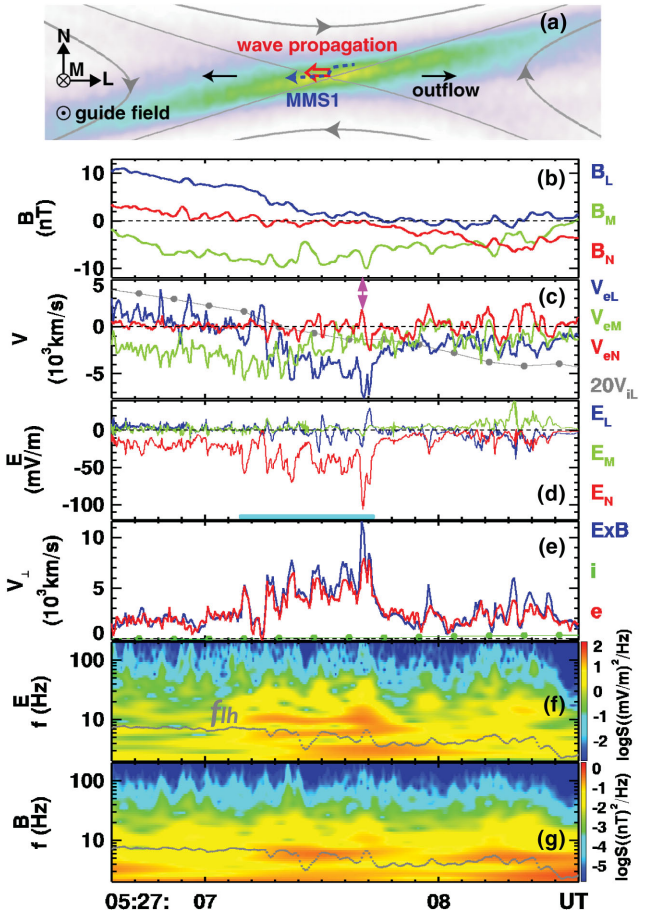

FIG. 1. Large-amplitude LHDWs driving electron flow bursts in an electron-scale reconnection layer detected by the MMS1 spacecraft. (a) Schematic showing MMS1 trajectory in an electron-scale current layer (the colored region where warmer colors represent stronger current densities) during reconnection with a guide field. Gray curves represent magnetic field lines. Note that the region where the outflow V_L is positive (negative), the magnetic field B_N is also positive (negative). (b) Three components of the magnetic field $\boldsymbol{B}$. (c) Electron flows V_{eLMN} and 20 times the ion outflow, $20V_{iL}$. (d) Electric field components E_{LMN}. (e) Electron (red) and ion (green) flow velocities along the $E \times B$ direction and the $E \times B$ drift speed (blue). (f) The electric field power spectral density. (g) The magnetic field power spectral density. The lower-hybrid wave frequency is displayed as a curve in panels (f) and (g). The wave interval is marked by a light blue bar in Fig. 1(d).

Large-amplitude waves in the lower-hybrid frequency range are observed in the electron current layer in the interval 05:27:07.15 − 05:27:07.75 UT [marked by a horizontal blue bar in Fig. 1(d)]. In this interval, B_M is the dominant magnetic component, known as the guide field, estimated to be ∼30% of the asymptotic reconnecting component [26]. The fluctuation profiles of the electron flow components V_{eL} and V_{eN} are correlated with those of the electric field components E_N and E_L, respectively, indicative of wave-driven flows through the $E \times B$ drift ($V_{E\times B}$). However, the electron flow velocity perpendicular

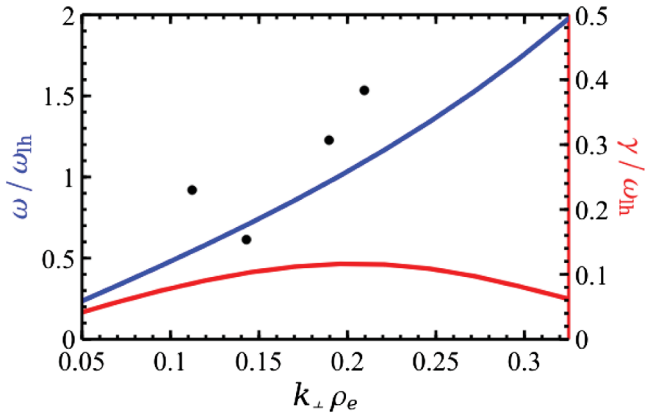

FIG. 2. The dispersion relation measured by MMS (solid black circles) and predicted by theory (blue curve) [10]. The MMS data points are observed at around the maximum growth rate (red) with an average $k_\perp \rho_e$ about 0.15. The electron thermal gyroradius $\rho_e = v_{te}/\omega_e \sim 8$ km, where the electron thermal speed $v_{te} = \sqrt{2T_e/m_e}$ is based on the average electron temperature T_e and the electron gyrofrequency ω_e based on the average magnetic field. The average lower-hybrid frequency $\omega_{lh} = 34$ rad/s.

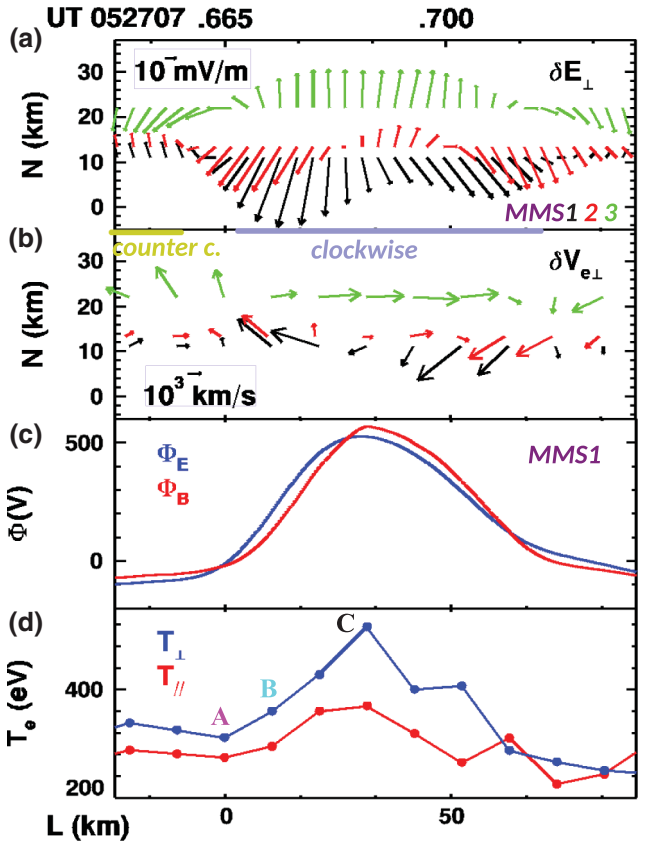

FIG. 3. One outstanding example of an LHDW structure (marked by the magenta arrow in Fig. 1) with its resulting electron vortical flow and heating. (a) Electric field vectors perpendicular to $\boldsymbol{B}$ projected onto the L-N plane from three MMS spacecraft. (b) Electron flows $\delta V_{e\perp}$ from three spacecraft showing a vortical pattern. (c) The electrostatic potentials Φ_E (blue) and Φ_B (red) computed based on integrating the measured $\delta E_\perp$ along $\boldsymbol{k}$ and based on δB, respectively. (d) Electron temperatures parallel (red) and perpendicular (blue) to $\boldsymbol{B}$ showing preferential perpendicular heating. The quantities $\delta E_\perp$, $\delta V_{e\perp}$, and δB are bandpass filtered at 2–50 Hz, extending beyond the range of the local f_{lh} to cover most of the enhanced $\boldsymbol{E}$ spectral power [Fig. 1(f)] while removing the dc component.

to the magnetic field ($V_{e\perp}$) exhibits finite deviations from $V_{E\times B}$ [Fig. 1(e)] in correlation with largest amplitude E fluctuations. The physics behind these deviations will be further studied in Fig. 4. The ion velocity $V_{i\perp}$ is much smaller than $V_{e\perp}$ and $V_{E\times B}$ [Fig. 1(e)], implying that ions are unmagnetized and decoupled from electrons. The decoupling gives rise to a strong ion-electron relative drift perpendicular to the magnetic field. This condition in combination with the density and magnetic field gradients along $\boldsymbol{N}$ is conducive to the LHDI [10]. The spectral powers in the electric [Fig. 1(f)] and magnetic [Fig. 1(g)] fields are enhanced by more than one order of magnitude in the lower-hybrid frequency range, $f_{lh} = \sqrt{f_{ci} f_{ce}} \sim 3$–$8$ Hz in the interval.

The frequency-wave number relation measured by MMS is consistent with the local dispersion relation predicted by the LHDI theory [10]. The MMS data points are observed at around the predicted maximum growth rate. The theoretical dispersion and the growth rate curves (Fig. 2) are obtained by inputting the parameters measured by MMS to Eq. (5) in Ref. [10] in the $T_e \ll T_i$ limit (the observed $T_e/T_i \sim 0.1$). The parameters (averaged over the wave interval) are the background $E \times B$ drift speed 4300 km/s, ion thermal speed 760 km/s, magnetic field magnitude 8.1 nT, plasma density 0.36 cm^{-3}, magnetic field gradient along N 0.20 nT/km, and density gradient along N −0.000 75 cm^{-3}/km. The ion bulk velocity $V_{i\perp}$ is negligible [see Fig. 1(e)] compared to the perpendicular wave speed $\omega/k_\perp \sim 1500$ km/s. The wave vector $\boldsymbol{k}$ for the f_{lh} range of 3–8 Hz (corresponding to the range of ω/ω_{lh} covered by the MMS data points in Fig. 2) is computed from the Fourier components of the measured magnetic field and current density at each frequency bin, $k(\omega) = i\mu_0 J(\omega) \times B^*(\omega)/|B(\omega)|^2$ [where $B^*(\omega)$ is the complex conjugate of $B(\omega)$], assuming traveling waves and no displacement current in Ampere's law [45]. The average direction of propagation is [−0.995, −0.071, 0.068] in the LMN coordinates, and average phase speed $\omega/k = 1450$ km/s.

Simultaneous multipoint measurements of the wave electric fields perpendicular to $\boldsymbol{B}$, denoted as $\delta E_\perp$, reveal an alternating converging and diverging pattern [an example is shown in Fig. 3(a)]. This pattern bears a high degree of similarity to the electric field structure of LHDW observed at a plasma boundary without reconnection [35]. The bandpass (2–50 Hz) filtered $\delta E_\perp$ vectors measured by MMS1-3 are projected onto the L-N plane using the propagation velocity $\boldsymbol{V}_p \sim -1450$ km/s$\hat{L}$ to

convert from time to distance along L [Fig. 3(a)]. The N coordinates are based on the spacecraft relative locations with zero set to be at the estimated $B_L = B_N = 0$ line (the reconnection X line).

In the presence of the guide field B_M, a vortical electron-flow pattern is formed on the L-N plane due to the $\delta E \times B$ drift. Here, the vortical $\delta V_{e\perp}$ flows are directly detected for the first time by the electron instrument on MMS and shown in Fig. 3(b). Such a flow pattern gives rise to a circulating perpendicular current and results in a magnetic perturbation δB along M. This δB is comparable to the guide field B_M, and can be visually discerned as the localized enhancement in B_M at 05:27:07.7 UT [marked by a magenta arrow in Fig. 1(c)]. The spatial scales of this vortical structure are approximately the half-width of the electron current layer ($\sim 2.8\, d_e$). The estimated half-width of the vortical structure is 30 km ($3.4\, d_e$) along L, and 15 km along N [Figs. 3(a) and 3(b)]. The N size is constrained by the spacecraft separation.

The LHDW dramatically impacts the electron dynamics in the reconnection layer. Electrons with gyroradius comparable with the half-width of the vortex are accelerated by the wave electric field, resulting in perpendicular heating and a possibility to enhance the tearing growth rate predicted by simulations, e.g., [7]. The electrostatic potential $\Phi_E = \int \delta E \cdot V_p dt$ reaches 560 V from the exterior to the center region of the vortical structure at 05:27:07.7 UT [Fig. 3(c)]. To determine $\boldsymbol{V}_p$, the potential can be written as $\Phi_B = B \cdot \delta B / en\mu_0$ [35,46] using Ampere's law $\nabla \times \delta B = \mu_0 en \nabla \Phi_B \times B/|B|^2$, where $\boldsymbol{B}$ is the instantaneous magnetic field, and the magnetic field perturbation δB (parallel to the average magnetic field over the vortex) is from the electron $\delta E \times B$ drift current. By maximizing the correlation between Φ_E and Φ_B profiles (correlation coefficient 0.97), the structure propagation velocity $\boldsymbol{V}_p$ is obtained to be -1430 km/s $\hat{L}$, consistent with the phase velocity obtained earlier. Figure 3(d) shows that the maximum increase in $T_{e\perp}$ is 205 eV in contrast to 96 eV for $T_{e\parallel}$. The potential provides a ~560 eV kinetic energy gain for the electrons passing from the equipotential of location A [locations are labeled on the data points in Fig. 3(d)] to that of location C within one gyro-orbit. In contrast, the average T_e for the interval 05:27:07.15 – 05:27:07.75 UT is 360 eV, significantly lower than the T_e inside the potential structure.

The perpendicular heating is nongyrotropic as revealed by the distribution functions. At the potential maximum, the electron distribution function in the velocity plane perpendicular to the magnetic field, the $v_{E\times B} - v_{E\perp}$ plane, exhibits a nongyrotropic crescent structure (distribution C in Fig. 4). The energy corresponding to the inner velocity boundary of the crescent population indicates the acceleration potential energy for electrons with negligibly small energy outside the potential structure, e.g., [47]. In this case, the inner boundary is at a cutoff speed of approximately 14 000 km/s (~558 eV), consistent with the potential energy difference 560 eV between locations A and C based on the electrostatic potential computed from the measured $\boldsymbol{E}$ and $\boldsymbol{B}$ [Fig. 3(c)]. This agreement indicates direct acceleration of the crescent electrons by the LHDW electrostatic potential. The crescent population has an angular spread with respect to $v_{E\perp} = 0$ due to finite gyroradius effects of nonuniformly distributed electrons that have been accelerated, e.g., [47–49]. Distribution A, located outside the potential, does not exhibit a crescent structure, supporting that the crescent distribution in Fig. 3 is a consequence of energization during electron gyration across the wave potential and not a mere product of the larger-scale reconnection process. In the wave interval, multiple vortices exhibiting nongyrotropic heating are observed.

As the spacecraft travels through the 2D potential structure along L, the maximally achievable kinetic

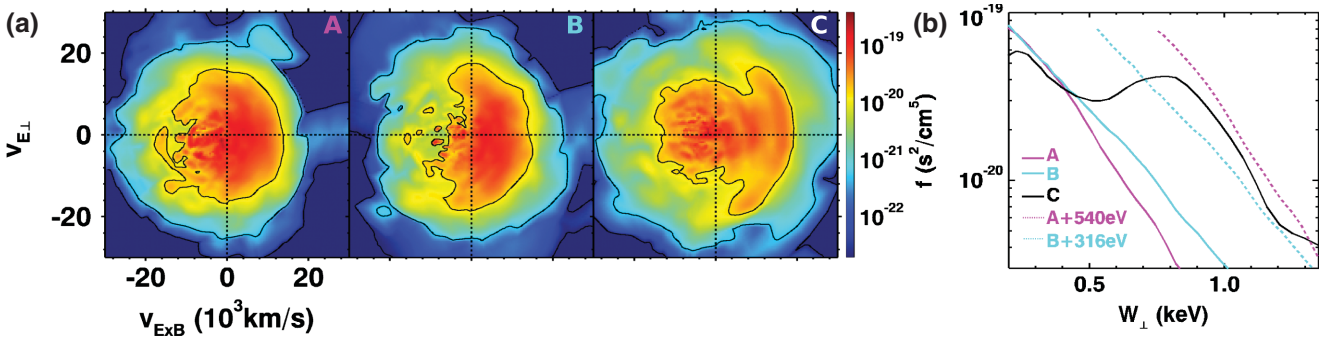

FIG. 4. Reduced electron distribution functions in the background $E \times B$ (low pass filtered fields below 1 Hz) drift frame showing nongyrotropic perpendicular heating and direct acceleration by the LHDW potential. (a) Distributions ABC [corresponding to the data points marked in Fig. 3(d)] in the $v_{E\times B} - v_{E\perp}$ plane, where $v_{E\times B}$ and $v_{E\perp}$ are along the $E \times B$ and perpendicular electric field directions, respectively. (b) Phase-space densities of the reduced distributions ABC as a function of the perpendicular energy $W_\perp$ along the direction of $v_{E\times B}$. The dotted magenta (light-blue) curve is distribution A (B) shifted by the potential energy difference between time A (B) and time C, and agrees with distribution C within uncertainties (±150 eV given by the instrument's energy bin width and/or the potential energy change over the distribution sampling time).

energies at locations A–C differ by the corresponding potential energy increments (Fig. 4), further supporting that the crescent electrons are demagnetized and accelerated by the LHDW potential. The phase-space density integrated over $v_\parallel$ and averaged over an angular range within 30° from the $+v_{E\times B}$ direction (approximately $-\hat{L}$) in the $v_\perp$ plane is plotted as a function of the electron perpendicular energy $W_\perp = m_e v_\perp^2/2$ [Fig. 4(b)]. The potential energy difference between time A (B) and time C [marked in Fig. 3(d)] deduced from Φ_E [Fig. 3(c)] is added to the spectra from distribution A (B) and plotted as the magenta (light blue) dotted curve. The agreement with spectra C between ~0.7–1.2 keV further substantiates that the crescent electrons are accelerated by the potential difference, implying that these electrons are demagnetized. The crescent electrons have an average energy ~800 eV. The gyroradius of these electrons from the edge ($|B| \sim 6$ nT) to the center ($|B| \sim 10$ nT) of the potential structure is 16–9 km. Electrons from outside of the potential could reach the peak potential region in one gyro-orbit, as the half-width of the potential is comparable to twice the gyroradius. We note that while the crescent electrons are demagnetized, the motion of lower energy electrons is predominantly the $\delta E_\perp \times B_M$ drift, and gives rise to the vortical flows.

The guide field plays a pivotal role in allowing LHDI to occur in the electron-scale reconnection layer. In the wave interval, the guide field (B_M) is the dominant magnetic field component [Fig. 1(a)], giving rise to a strong electron outflow jet V_{eL} through the $E_N \times B_M$ drift in the high Hall electric field E_N region [Figs. 1(c)–1(e)]. The background drift velocity is toward $-L$ with an averaged magnitude of 4300 km/s (~15 V_A, based on local $|B|$), placing the system in a high drift regime as this electron-ion relative drift is significantly larger than the ion thermal speed of 750 km/s. The guide field keeps the electron beta (ratio of the electron thermal energy to the magnetic energy) in the range of ~0.3–2 during the LHDW interval, such that the finite-beta stabilization [10] does not come into effect. The relatively high electron-ion drift and moderate beta due to the guide field provide an environment for LHDI to take place.

In summary, LHDWs are observed to cause electron nongyrotropic heating and vortical flows in an electron-scale reconnection layer with a finite guide field. The waves have a spatial scale comparable to the half-width of the electron layer, and primarily propagate along the outflow direction. Electron preferential perpendicular heating and nongyrotropy predicted by simulations [7] are observed for the first time, providing a potentially fertile ground for further reconnection to occur on the wave spatial scales. The strong electron vortical flows lead to δB comparable to the guide field magnitude. The measurements reveal a new regime of LHDW interaction with electrons.

Can the preferential perpendicular heating further trigger secondary tearing at the LHDW scale? Pursuit of this open question will transform our current picture of turbulent reconnection and guide-field reconnection. Existing analysis of tearing instabilities considers primarily current sheets much thicker than the electron scale. To address the question of reconnection onset on the LHDW scale, fully kinetic simulations and state-of-the-art laboratory reconnection experiments that resolve the plasma response in the LHDW spatiotemporal scales are required.

The work was supported by NSF Grants No. AGS-1619584 and No. AGS-1552142, DOE Grant No. DESC0016278, NASA Grants No. 80NSSC18K1369 and No. 80NSSC17K0012, and the NASA MMS mission. MMS data are available at the MMS Science Data Center.

[1] J. F. Drake, J. Gerber, and R. G. Kleva, J. Geophys. Res. **99**, 11211 (1994).
[2] R. G. Kleva and J. F. Drake, Phys. Fluids **27**, 1686 (1984).
[3] A. Le, W. Daughton, L.-J. Chen, and J. Egedal, Geophys. Res. Lett. **44**, 2096 (2017).
[4] A. Le, W. Daughton, O. Ohia, L.-J. Chen, Y.-H. Liu, S. Wang, W. D. Nystrom, and R. Bird, Phys. Plasmas **25**, 062103 (2018).
[5] D. B. Graham *et al.*, J. Geophys. Res. **122**, 517 (2016).
[6] I. H. Cairns and B. F. McMillan, Phys. Plasmas **12**, 102110 (2005).
[7] P. Ricci, J. U. Brackbill, W. Daughton, and G. Lapenta, Phys. Plasmas **11**, 4489 (2004).
[8] J. D. Huba, N. T. Gladd, and K. Papadopoulos, Geophys. Res. Lett. **4**, 125 (1977).
[9] J. D. Huba, N. T. Gladd, and K. Papadopolulos, J. Geophys. Res. **83**, 5217 (1978).
[10] R. C. Davidson, N. T. Gladd, C. S. Wu, and J. D. Huba, Phys. Rev. Lett. **37**, 750 (1976).
[11] L.-J. Chen, A. Bhattacharjee, P. A. Puhl-Quinn, H. Yang, N. Bessho, S. Imada, S. Muhlbachler, P. W. Daly, B. Lefebvre, Y. Khotyaintsev *et al.*, Nat. Phys. **4**, 19 (2008).
[12] M. Yamada, L.-J. Chen, J. Yoo, S. Wang, W. Fox, J. Jara-Almonte, H. Ji, W. Daughton, A. Le, J. Burch *et al.*, Nat. Commun. **9**, 5223 (2018).
[13] L.-J. Chen, N. Bessho, B. Lefebvre, H. Vaith, A. Fazakerley, A. Bhattacharjee, P. A. Puhl-Quinn, A. Runov, Y. Khotyaintsev, A. Vaivads, E. Georgescu, and R. Torbert, J. Geophys. Res. **113**, A12213 (2008).
[14] L.-J. Chen, N. Bessho, B. Lefebvre, H. Vaith, A. Asnes, O. Santolik, A. Fazakerley, P. Puhl-Quinn, A. Bhattacharjee, Y. Khotyaintsev, P. Daly, and R. Torbert, Phys. Plasmas **16**, 056501 (2009).
[15] L.-J. Chen, W. S. Daughton, B. Lefebvre, and R. B Torbert, Phys. Plasmas **18**, 012904 (2011).
[16] L.-J. Chen, W. Daughton, A. Bhattacharjee, R. B. Torbert, V. Roytershteyn, and N. Bessho, Phys. Plasmas **19**, 112902 (2012).
[17] M. Fujimoto, I. Shinohara, and H. Kojima, Space Sci. Rev. **160**, 123 (2011).

[18] T. A. Carter, M. Yamada, H. Ji, R. M. Kulsrud, and F. Trintchouk, Phys. Plasmas **9**, 3272 (2002).
[19] T. A. Carter, H. Ji, F. Trintchouk, M. Yamada, and R. M. Kulsrud, Phys. Rev. Lett. **88**, 077201 (2002).
[20] I. Shinohara, T. Nagai, M. Fujimoto, T. Terasawa, T. Mukai, K. Tsuruda, and T. Yamamoto, J. Geophys. Res. **103**, 20365 (1998).
[21] S. D. Bale, F. S. Mozer, and T. Phan, Geophys. Res. Lett. **29**, 2180 (2002).
[22] H. Ji, S. Terry, M. Yamada, R. Kulsrud, A. Kuritsyn, and Y. Ren, Phys. Rev. Lett. **92**, 115001 (2004).
[23] H. Ji, R. Kulsrud, W. Fox, and M. Yamada, J. Geophys. Res. **110**, A08212 (2005).
[24] J. L. Burch, R. B. Torbert, T. D. Phan, L.-J. Chen, T. E. Moore, R. E. Ergun, J. P. Eastwood, D. J. Gershman, P. A. Cassak, M. R. Argall *et al.*, Science **352**, aaf2939 (2016).
[25] D. B. Graham, Y. V. Khotyaintsev, C. Norgren, A. Vaivads, M. Andre, J. F. Drake, J. Egedal, M. Zhou, O. Le Contel, J. M. Webster *et al.*, J. Geophys. Res. **124**, 8727 (2019).
[26] L.-J. Chen, S. Wang, M. Hesse, R. E. Ergun, T. Moore, B. Giles *et al.*, Geophys. Res. Lett. **46**, 6230 (2019).
[27] A. C. Rager, J. C. Dorelli, D. J. Gershman, V. Uritsky, L. A. Avanov, R. B. Torbert *et al.*, Geophys. Res. Lett. **45**, 578 (2018).
[28] W. Daughton, Phys. Plasmas **10**, 3103 (2003).
[29] W. Daughton, G. Lapenta, and P. Ricci, Phys. Rev. Lett. **93**, 105004 (2004).
[30] I. Shinohara and M. Fujimoto, Cospar Colloq. Ser. **16**, 123 (2005).
[31] K. G. Tanaka, I. Shinohara, and M. Fujimoto, Geophys. Res. Lett. **32**, L17106 (2005).
[32] P. H. Yoon, A. T. Y. Lui, and M. I. Sitnov, Phys. Plasmas **9**, 1526 (2002).
[33] J. Ng, A. Hakim, J. Juno, and A. Bhattacharjee, J. Geophys. Res. **124**, 3331 (2019).
[34] M. Tanaka and T. Sato, J. Geophys. Res. **86**, 5541 (1981).
[35] C. Norgren, A. Vaivads, Yu. V. Khotyaintsev, and M. Andre, Phys. Rev. Lett. **109**, 055001 (2012).
[36] C. T. Russell, B. J. Anderson, W. Baumjohann, K. R. Bromund, D. Dearborn, D. Fischer *et al.*, Space Sci. Rev. **199**, 189 (2016).
[37] O. LeContel, P. Leroy, A. Roux, C. Coillot, D. Alison, A. Bouabdellah *et al.*, Space Sci. Rev. **199**, 257 (2016).
[38] R. E. Ergun, S. Tucker, J. Westfall, K. A. Goodrich, D. M. Malaspina, D. Summers *et al.*, Space Sci. Rev. **199**, 167 (2016).
[39] P.-A. Lindqvist, G. Olsson, R. B. Torbert, B. King, M. Granoff, D. Rau *et al.*, Space Sci. Rev. **199**, 137 (2016).
[40] C. Pollock, T. Moore, A. Jacques, J. Burch, U. Gliese, Y. Saito *et al.*, Space Sci. Rev. **199**, 331 (2016).
[41] See Supplemental Material at http://link.aps.org/supplemental/10.1103/PhysRevLett.125.025103 for the magnetic field and density profiles from the upstream to the electron-scale reconnection layer, which includes Refs. [42–44].
[42] B. U. Ö. Sonnerup and L. J. Cahill, Jr., J. Geophys. Res. **72**, 171 (1967).
[43] A. V. Khrabrov and B. U. Ö. Sonnerup, Geophys. Res. Lett. **25**, 2373 (1998).
[44] C. C. Harvey, in *Spatial Gradients and the Volumetric Tensor*, edited by G. Paschmann and P. W. Daly (ISSI/ESA, Noordwijk, Netherlands, 1998).
[45] P. M. Bellan, J. Geophys. Res. **121**, 8589 (2016).
[46] A. Divin, Yu. V. Khotyaintsev, A. Vaivads, and M. Andre, J. Geophys. Res. **120**, 1124 (2015).
[47] N. Bessho, L.-J. Chen, and M. Hesse, Geophys. Res. Lett. **43**, 1828 (2016).
[48] J. R. Shuster, L.-J. Chen, M. Hesse, M. R. Argall, W. Daughton, R. B. Torbert, and N. Bessho, Geophys. Res. Lett. **42**, 2586 (2015).
[49] L.-J. Chen, M. Hesse, S. Wang, N. Bessho, and W. Daughton, Geophys. Res. Lett. **43**, 2405 (2016).